DTU Library

Assessing fluctuating wind to hydrogen production via long-term testing of solid oxide electrolysis stacks

Liu, Hua; Høgh, Jens; Blennow, Peter; Sun, Xiufu; Zong, Yi; Chen, Ming

Published in:
Applied Energy

Link to article, DOI:
10.1016/j.apenergy.2024.122938

Publication date:
2024

Document Version
Publisher's PDF, also known as Version of record

Applied Energy 361 (2024) 122938

Contents lists available at ScienceDirect

Applied Energy

journal homepage: www.elsevier.com/locate/apenergy

Assessing fluctuating wind to hydrogen production via long-term testing of solid oxide electrolysis stacks

Hua Liu [a], Jens Høgh [a,b], Peter Blennow [b], Xiufu Sun [a], Yi Zong [c], Ming Chen [a,*]

[a] *Department of Energy Conversion and Storage, Technical University of Denmark, 2800 Kgs. Lyngby, Denmark*
[b] *Topsoe A/S, Haldor Topsøes Alle 1, 2800 Kgs. Lyngby, Denmark*
[c] *Department of Wind and Energy Systems, Technical University of Denmark, 4000 Roskilde, Denmark*

HIGHLIGHTS

- A 2104 h SOEC stack test with simulated fluctuating wind power input was conducted.
- Deployed constant flow and constant conversion strategies in the dynamic period.
- The Topsoe stack is robust and flexible for harsh and varying working environments.
- Fluctuations didn't introduce extra degradation in the current test.

ARTICLE INFO

Keywords:
Solid oxide electrolysis cell
SOEC stack
Operation strategy
Hydrogen production
Wind energy
Dynamic operation

ABSTRACT

The Danish government plans two energy islands to collect offshore wind power for power distribution and green fuel production. Wind power is often criticized for lacking stability, which challenges downstream fuel synthesis processes. Solid oxide electrolysis cells (SOEC) are promising for green hydrogen production on a commercial scale, but the impact of fluctuating power on SOEC remains uncertain. This paper explores the feasibility of a Wind-SOEC coupled system by conducting a 2104-h durability test with the state-of-the-art Topsoe TSP-1 stack. Three periods of steady operation and two periods of dynamic operation were conducted. Wind power fluctuation was simulated during the dynamic period, and two control strategies were used to handle it. The constant flow (CF) and constant conversion (CC) strategies maintain the feedstock flow rate and conversion ratio of steam-to-hydrogen, respectively. Compared to steady operation, the stack shows no signs of additional degradation in dynamic operation. Thus, the TSP-1 stack has been proven robust and flexible enough to handle fluctuating wind power supplies under both operation strategies. Further, stack performance during dynamic periods was compared and analyzed by removing degradation effects. Accordingly, SOEC stacks with CC control will consume less external heat than CF to maintain a heat balance. Nevertheless, SOEC systems with CF and CC control strategies may have different efficiency or hydrogen production costs. Tech-economic analyses will be needed to investigate control strategies at the system level.

1. Introduction

As a pioneer, Denmark has set one of the world's most ambitious goals: to reduce greenhouse gas (GHG) emissions by 70% in 2030 (compared to 1990) [1]. Despite the recent energy crisis, the government was more ambitious by pushing the net zero target from 2050 to 2045 [2]. The Danish coast has rich wind resources and shallow water depths. It is suitable for and will build large-scale offshore wind farms to support the net zero target. Offshore wind power is a vital renewable energy resource undergoing rapid development, including lower power production costs, higher wind energy conversion efficiency, better reliability, etc. [3]. Its advantages include a higher capacity factor and fewer installation restrictions on view or height [4]. The Danish government plans to build two energy islands in the Baltic and North Seas to boost offshore wind power [5]. Nordic Energy Island is an artificial island that collects electricity from nearby offshore wind farms. Centralized transmission systems can integrate more distant offshore wind power through shorter submarine cables and lower costs [5,6]. The

* Corresponding author.
E-mail address: minc@dtu.dk (M. Chen).

https://doi.org/10.1016/j.apenergy.2024.122938
Received 6 November 2023; Received in revised form 31 January 2024; Accepted 25 February 2024
Available online 10 March 2024

Baltic Energy Island (Bornholm) has a similar function and is described in Section 2.

Wind power collected on the islands can produce green fuel for maritime transportation after fulfilling land user demand. Hydrogen is one of the green fuel candidates for the maritime sector. It is volatile, flammable, and expensive to store, but has no color, smell, toxicity, or carbon emissions [7]. Hydrogen or hydrogen carriers have higher energy density than batteries and lower energy density than traditional heavy oil. According to the International Maritime Organization's (IMO) greenhouse gas (GHG) strategy, ships should implement green fuel by 2030 and eventually reach net zero emissions by 2050 [8]. However, the maritime sector is sensitive to fuel prices. A cheap green fuel on the market will encourage shipowners to use it and decarbonize maritime transportation. Therefore, wind-to-hydrogen production processes must be energy-efficient and cost effective to reduce hydrogen production costs.

Wind power is often criticized for lacking stability to produce hydrogen because wind speed fluctuates, and wind turbine inertia is moderate [9]. Power variations are affected by power capacity, rate of change, location, and other factors [10]. Downstream green hydrogen production systems must convert electricity into chemical energy with fluctuations and low-quality power supplies. Water or steam electrolysis processes can generate hydrogen effectively from unstable power sources, including wind power. There are several water electrolyzer designs with different catalysts and mechanisms, such as Alkaline Electrolysis Cell (AEC), Proton Exchange Membrane Electrolysis Cell (PEMEC), and Solid Oxide Electrolysis Cell (SOEC) [11]. AEC uses an alkaline solution as the electrolyte to conduct hydroxide ions at 60 ∼ 90 °C and a wide range of pressures. PEMEC transports protons through the membrane and splits water with expensive noble metal catalysts at 50–100 °C. The operating pressure of commercial PEMEC is usually between 30 and 40 bars. High-pressure PEMEC up to 350 or 700 bar is under development for direct compressed hydrogen storage [12]. SOEC is being commercialized for large-scale energy storage and clean fuel production [11,13]. Its electrolyte is an anion membrane that allows oxygen ions to pass through. SOEC operates at an elevated temperature of 650 ∼ 800 °C. Operating pressure is usually 1 bar, but high-pressure operations have been tested, and SOEC had solid performance under pressurization operation [14]. Electrolysis technologies are competing for a greater share of the green hydrogen market. Positive progress has been made, as megawatt-scale projects for each technology have been announced, installed, or operated. The desire for a green society and a growing demand have brought industry and academia together to develop electrolysis technologies for specific application backgrounds.

These three electrolysis technologies have been tested and modeled under dynamic realistic scenarios, which include grid disturbances, blackouts, renewable energy fluctuation, etc. [15–17]. A cycle test was conducted on a PEMEC cell to reveal the impact of periodic variation between 0–2 A [18]. Reduced currents or periodic interruptions can increase PEMEC durability. Real-life fluctuations differ from hypothetical cycles since power in the field varies with frequency and amplitude. An AEC stack was tested with real-world wind power dynamic profiles for over 4000 h (about six months) [19]. Even though dynamic operation causes some additional polarization, the stack has shown promising stability in producing hydrogen under power fluctuation. The SOEC has been subjected to on/off cycle tests and dynamic simulations [20,21]. However, the impact of wind power fluctuations on the SOEC stack regarding potential challenges and solutions remains uncertain.

Two factors should be closely monitored during the SOEC fluctuation durability test: degradation and heat management. Degradation increases SOECs' polarization and resistance. Potential degradation mechanisms include Ni coarsening or migration in the cathode, phase transformation of the electrolyte, secondary phase formation near the anode, etc. [22–24]. Through degradation, more electricity is converted into joule heat rather than chemical energy, making SOECs less efficient. Besides, SOEC cells are fragile under large temperature gradients, making heat management critical. A temperature gradient of >10 K cm^{-1} could cause delamination or cracking and should be eliminated to prevent failure [25]. Steam splitting and electronic transport resistance are heat sinks and sources, respectively. The heat sink and source are balanced at thermoneutral voltage (∼1.29 V), leading to minor temperature gradients. When SOECs run below/above thermoneutral voltage, less/more joule heat is released, causing a temperature drop/increase. Besides, degradation increases resistance and emits more joule heat after long-term operation. The complex heat balancing situation calls for both heat producers and carriers. Hot plates or pre-heaters supply external electric heat to the SOEC stack independently. Air on the anode side carries additional heat away and cools down stacks. It can also take external heat from pre-heaters to SOECs. However, an excessive air flow rate increases the size and capital cost of the heat exchanger and system. Optimizing the maximum air flow rate is necessary for economic concerns. As a result, proper flow rate and heater duty control will minimize temperature gradients and make SOEC system flexible and less expensive. Monitoring SOEC degradation and heat balance in the durability tests will facilitate industrial applications by providing more information.

Typically, wind-powered SOEC systems operate at part-load since they are designed with the highest capacity. Therefore, the SOEC operation strategy should maximize system efficiency during fluctuating power supply. Meanwhile, the electric steam generator is the most energy-intensive component of the SOEC Balance of Plant (BoP) [22]. A proper water/steam flow rate control strategy is thus essential to save renewable energy and improve system efficiency. Constant flow (CF) and constant conversion ratio (CC) are flow rate control strategies for the SOEC cathode inlet (mixture of steam and diluted hydrogen). CF maintains the inlet flow rate, while CC updates it based on the power supply and hydrogen production. Both strategies have been simulated for a part-load SOEC system but have not yet been tested in the lab [26]. Experiments on flow rate operation strategies are necessary to understand SOEC behavior and system requirements. Testing flow rate operation strategies will provide insight into the SOEC stack, potential challenges, limitations of the system components, etc.

In this work we conduct a 2104 h long-term test to clarify the impact of fluctuating wind power and control strategy on the SOEC stack. The dynamic performance of the SOEC stack is investigated under a realistic wind power profile. The following section introduces wind speed profiles and wind farm power generation on Bornholm Island before detailing experiment setup and control strategies. Two control strategies, CF and CC, are tested to simulate the system response to wind power fluctuations. Dynamic long-term experiment data will be presented at cell and stack levels, including voltage and temperature. Further discussion of degradation and heat balance will confirm whether the stack is robust enough for dynamic operation.

2. Baltic Energy Island - Bornholm

The Danish government plans to make Bornholm, a Danish island in the Baltic Sea, an energy hub to distribute offshore wind power. Until 2020, the Bornholm power distribution system comprises about 28,000 electricity customers with a 55 MW peak load. Current clean energy sources include wind power (37 MW), combined heat and power (CHP, 13 MW), and photovoltaic (PV, approximately 23 MW). Planned offshore wind farms will be installed about 15 km south-southwest of the coast without obstructing the horizon view [5]. The offshore wind power will have a capacity up to 3.8 GW, equivalent to the energy consumption of 3.3 million homes. The energy island will also contribute to the EU since the Bornholm power system is connected to Sweden, Germany, and Denmark (Zealand) via sea cables (see Fig. 1). Currently, clean electricity is used by local customers and supplied to the DK2 Nord Pool power market by the Nordic interconnected system [27], and the new bidding zone (DK3) will enter into force when Bornholm Energy Island is in operation [28]. Excess wind power collected on the

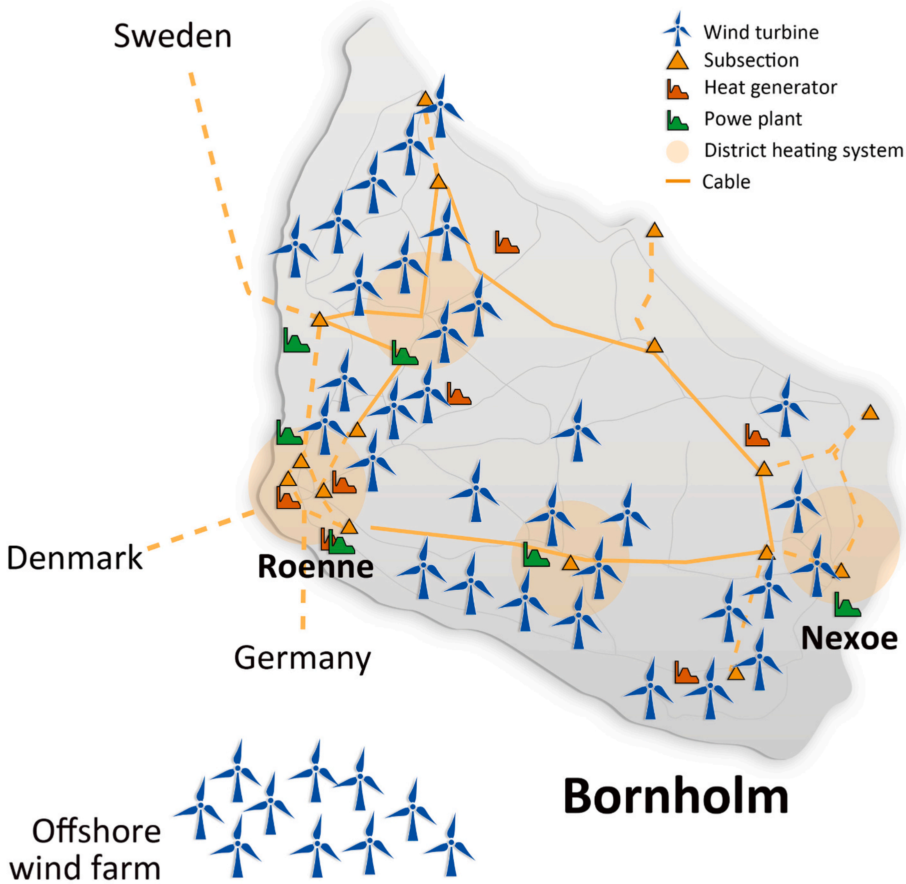

Fig. 1. Illustration of the Bornholm power distribution system. The figure was modified with permission from [29], Copyright 2019 Elsevier. A recent offshore wind farm development plan [5] was involved.

islands could be converted into green hydrogen and used directly (or converted to hydrogen carriers) as fuel for cars, trucks, ships, etc.

Local atmospheric activity repeats yearly, and local wind power probability in the future could be predicted from historical profiles. Fig. 2 presents the historical wind speed and power in 2013 and December from one selected wind farm in Bornholm. The recorded data has a five-minute resolution. Histograms of wind power and wind power change per five minutes are also included. The maximum wind speed in December was 21.9 $m \cdot s^{-1}$, also the maximum that year. Wind speed and power generation are not linearly related. Wind turbines generate less electricity at a slower wind speed. Power generation varies dramatically when the wind blows between 5 and 10 $m \cdot s^{-1}$. When the wind speed exceeds 14 $m \cdot s^{-1}$, the wind turbine will be stopped by blade control and no longer produce power. More details about the wind farm power generation efficiency curve can be found in [30,31].

The maximum wind power generation of the selected Bornholm wind farm is 12.5 MW, and the yearly average is 2.77 MW, while the December monthly average is 5.39 MW. Probability distribution (p) of yearly wind power peaks at lower power levels. $p(P < 1\ \text{MW})$ is 48.2%, and $p(P > 11\ \text{MW})$ is 4.7%. Wind power profiles in December differ from those in the whole year. There are two peaks in the probability distribution of monthly wind power, one at the bottom and one at the top. Low power generation exhibits more probability, with $p(P < 1\ \text{MW})$ being 21.9%, while $p(P > 11\ \text{MW})$ is 16.8%.

Wind power variation indicates the amplitude of the fluctuation and the disturbance to the SOEC stack. The power variation is converted to per unit (pu) by dividing the nominal value (12.5 MW). Over the year, 59% of the disturbances occur within 0.01 $pu \cdot 5\ min^{-1}$, with the highest of 0.35 $pu \cdot 5\ min^{-1}$. However, the probability of extreme variation $p(dP > 0.2\ pu \cdot 5\ min^{-1})$ is 0.14‰, which is negligible. Monthly power variation has a 43.4% likelihood of <0.01 $pu \cdot 5\ min^{-1}$, with the highest of 0.23 $pu \cdot 5\ min^{-1}$. A long tail probability of extreme variation $p(dP > 0.2)$ is also negligible at 0.22‰. The power change is more significant in December than throughout the year. The monthly power change average is 0.017 $pu \cdot 5\ min^{-1}$, while the yearly average is 0.024 $pu \cdot 5\ min^{-1}$. Fast and large deviates in the wind profile could pose a challenge to the SOEC stack and/or system.

3. Experimental

In this work a fresh 75-cell state-of-the-art Topsoe SOEC stack, the Topsoe Stack Platform (TSP-1), was employed for the durability test. [32,33] The stack comprises planar-type Ni/Yttria-stabilized zirconia (YSZ) electrode-supported cells connected by interconnects made of Crofer22APU with a protective coating on both sides. Each cell has an active area of 109 cm^2. Further details about the cells and TSP-1 stacks can be found elsewhere [34,35]. A recent 4000-h ramp, cycle, and restart test validated the stability of TSP-1 stacks in the electric grid [36]. Inside the stack, the 75 cells have been grouped into 13 groups: 12 groups with six cells, 1 group with three cells (middle group), named G01–13, and G01 at the bottom. Voltage probes in contact with the interconnect plates were used to monitor the voltage in each group. Measured voltage includes contributions from the cells, the interconnects, and the connection between them within that group. Four thermocouples are inserted into the stack gas channels, two for cathode streams (cathode inlet and outlet) and two for anode streams (anode inlet and outlet). The stack average temperature is estimated as the mean value of four gas channel temperatures. The TSP-1 stack was placed in the oven during the actual testing, and an electric heater maintained the furnace temperature at about 750 °C. External heat is

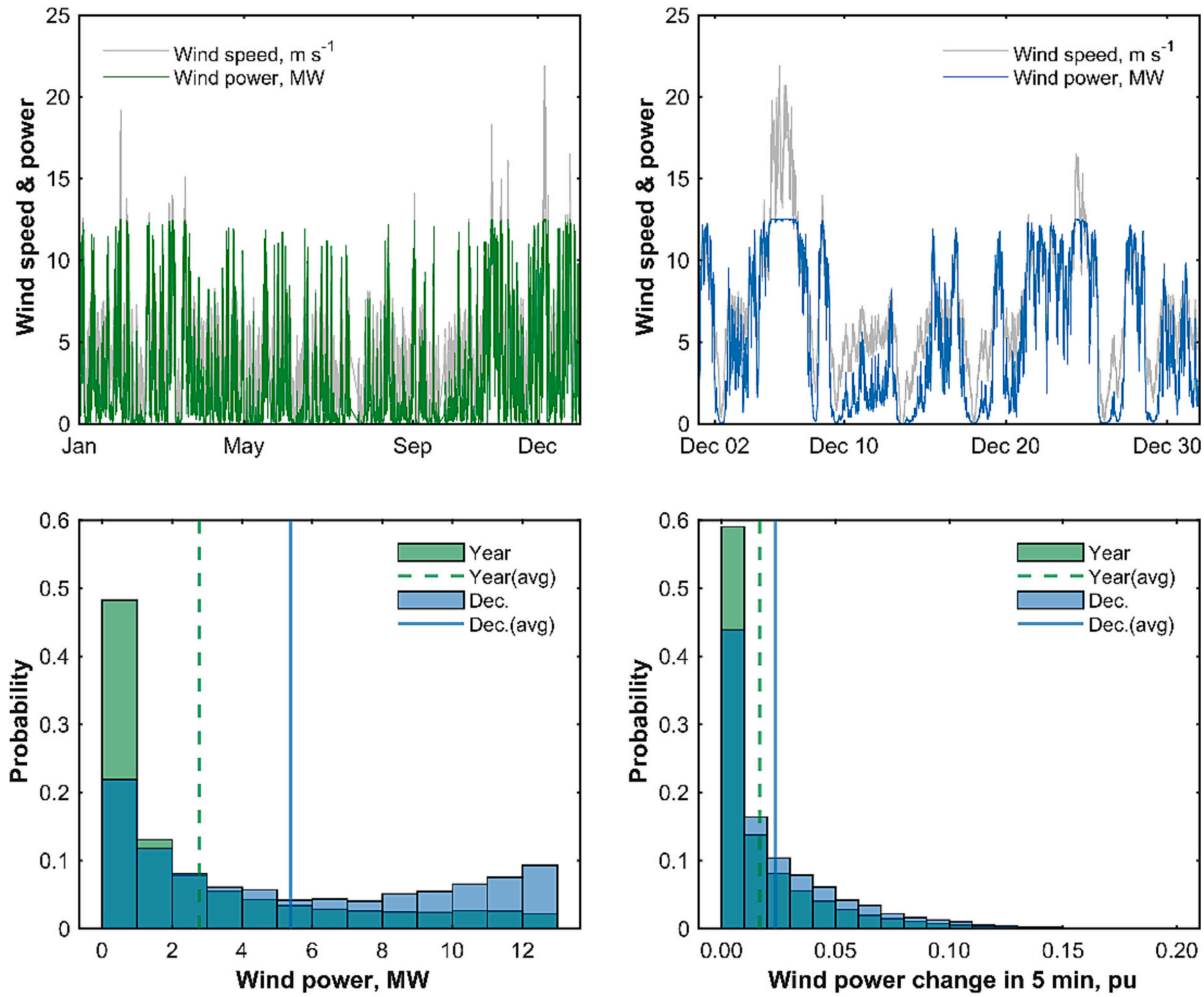

Fig. 2. Wind speed and power profiles for the entire 2013 (left) and for the December month in 2013 (right) are shown in the top figures. Histograms of wind power (left) and the absolute value of wind power change per 5 min (right) are shown in the bottom figures. Vertical solid and dashed lines represent yearly and monthly averages, respectively.

transferred from the oven to the SOEC stack to compensate for endothermic reaction heat. Oven heat duty is kept at a specific value, determined by achieving the desired stack average temperature before the durability test. An electric steam generator evaporates water according to a flow rate control signal. The pre-heater elevates the steam temperature with constant duty before sending it into the stack. Detailed parameters and responses during the fluctuating long-term test are listed in Table 1.

Table 1
Parameters for the SOEC stack fluctuating long-term test.

Name	Unit	CF	CC
Total test time	h	746	747
Time per segment	min	5	15
Number of segments	–	8928	2976
Max. current density	$A{\cdot}cm^{-2}$	0.50	0.50
Avg. current density	$A{\cdot}cm^{-2}$	0.23	0.26
Min. current density	$A{\cdot}cm^{-2}$	0.10	0.10
Max. H_2O-to-H_2 conversion ratio	%	55.7	35.4
Avg. H_2O-to-H_2 conversion ratio	%	26.1	27.2
Min. H_2O-to-H_2 conversion ratio	%	11.1	14.5
Max. H_2 production rate	$Nm^3{\cdot}h^{-1}$	1.71	1.71
Avg. H_2 production rate	$Nm^3{\cdot}h^{-1}$	0.82	0.82
Min. H_2 production rate	$Nm^3{\cdot}h^{-1}$	0.34	0.34
Total H_2 production	Nm^3	618	612
Total power consumption	kWh	1772	1839
Avg. power consumption	kW	2.25	2.72
	$kWh{\cdot}Nm^{-3}\ H_2$	2.75	2.76

The SOEC stack was conditioned, reduced, and characterized according to the Topsoe stack testing procedure. A 2104-h durability test was conducted over five periods under different operating conditions. There are three short-term steady operation periods (BL1, BL2, and BL3) plus two 744-h fluctuating operation periods (CF and CC). Testing begins with a stable operation, followed by alternating dynamic and stable operations in the following order: BL1-CF-BL2-CC-BL3. Fig. 3 shows the flow rate and conversion ratio for the entire test, while Fig. 4 shows the current density profile/histogram of the dynamic periods. SOEC stacks may have substantial degradation at high power loads with large current density or conversion ratios [37]. To focus on dynamic performance, stack duty is kept at a low level during the durability test.

3.1. Baseline (BL)

Under steady operation, the stack was tested at 725 °C, and an electrolysis current density (i) of 0.24 $A{\cdot}cm^{-2}$,[1] with H_2O/H_2 (90/10)

[1] The current density of the electrolysis reaction is usually marked as negative to emphasize the opposite current direction to that of fuel cell mode operation. For convenience, the electrolysis reaction current and current density are marked as positive in this paper.

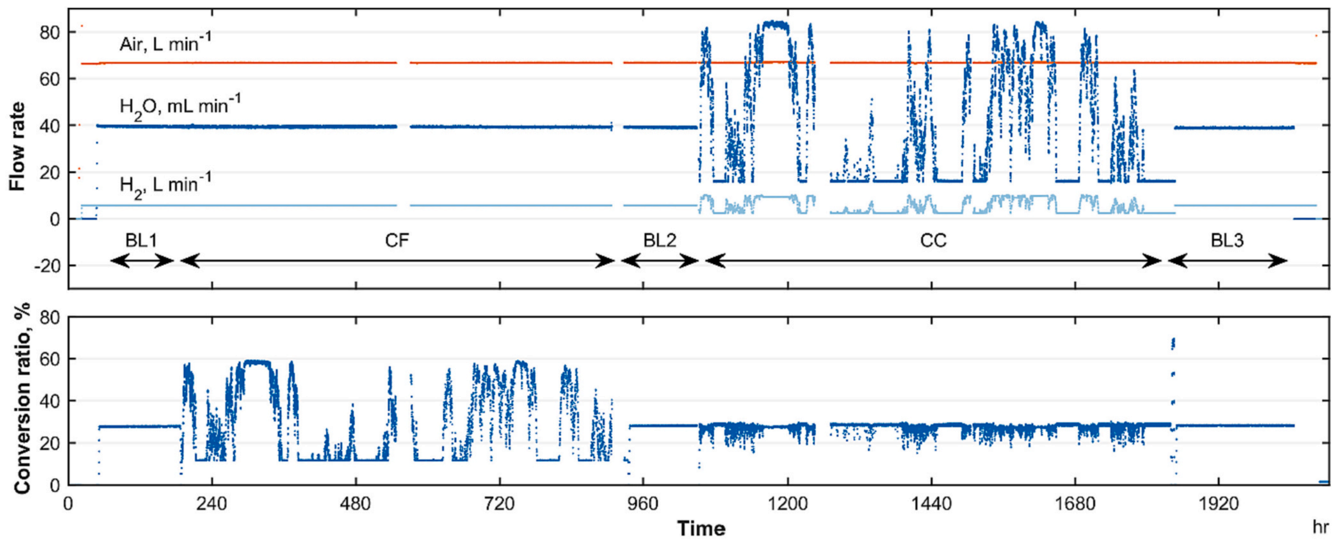

Fig. 3. Evolution of the flow rate (top) and conversion ratio (bottom) during the fluctuating durability test.

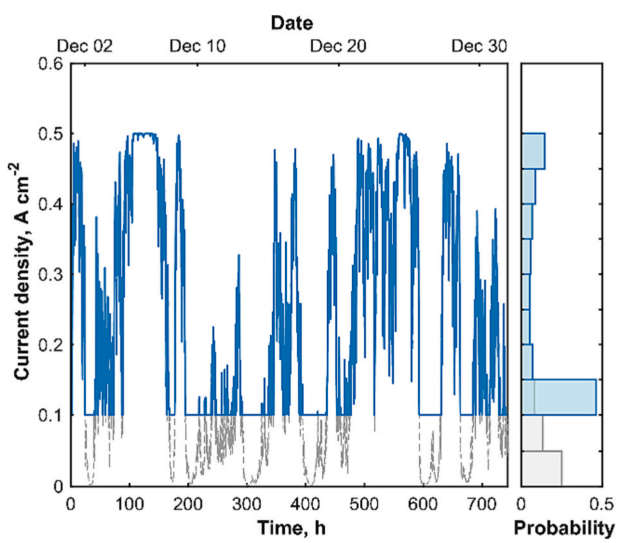

Fig. 4. SOEC stack current density in dynamic operation is shown as a blue solid line. The gray dash line is the current density without a lower limit. The histogram of the current density w/wo lower limitation is shown in the right figure. (For interpretation of the references to color in this figure legend, the reader is referred to the web version of this article.)

supplied to the hydrogen electrode and air to the oxygen electrode. Some hydrogen is introduced to dilute the steam to prevent Ni oxidation at the cathode electrode. The liquid water flow rate was fixed at 39.7 mL·min^{-1}, resulting in an H_2O-to-H_2 conversion ratio of 27%. H_2 and air flow rates were controlled at 5.67 L·min^{-1} and 66.5 L·min^{-1}, respectively. Volume flow controllers were used to control the flow rate of gas and liquid at room temperature and atmospheric pressure. Steady operation is used as a baseline (BL) to present stack performance without wind fluctuation.

3.2. Constant Flow (CF)

In dynamic operation periods, the stack follows the December wind power profile, simulating converting all wind power output to hydrogen. The wind profile in Fig. 2 is down-scaled to what the TSP-1 stack can handle (about 7 kW). An electrolysis current density fluctuating between 0.1 and 0.5 A·cm^{-2} was applied to the stack, as shown in Fig. 4. Such treatment increase $p(i < 0.15$ A·cm$^{-2})$ to 46.5% and maintains the probability of the rest current density. Similar to the wind speed probability distribution, there is another peak at full load $p(i > 0.45$ A·cm$^{-2})$ of 14.6%. The minimum current density is limited to emphasize long-term voltage variation and degradation behaviors at reduced stack duty. Even so, stack operation below 0.1 A·cm^{-2} is feasible in field operations with CF control but not tested.

The gas flows were kept constant within the CF period, while the current density followed the wind profile. Water/steam, hydrogen, and air flow rates were maintained as BL. As a result, the H_2O-to-H_2 conversion ratio *SC* is:

$$SC = \frac{\dot{n}_{\mathrm{react}}}{\dot{n}_{\mathrm{H_2O}}} = \frac{I_{\mathrm{stack}}}{2F\dot{n}_{\mathrm{H_2O}}} \tag{1}$$

where I is current, F is Faraday constant, $\dot{n}$ is molar flow rate in mol·s^{-1}, and $\dot{n}_{\mathrm{react}}$ is hydrogen molar production rate. Thus, the current density variation altered the conversion ratio thus outlet gas composition. As a result, the *SC* varied between 11.1% and 55.7%, with a constant steam flow rate during the CF period. There were 8928 segments within the CF period, as the operation was turned every five minutes. Between every two segments, the maximum current density decreasing or increasing was 0.095 A·cm^{-2} and 0.094 A·cm^{-2}, respectively.

3.3. Constant Conversion (CC)

Water evaporation is energy intensive. Therefore, minimizing the liquid water flow rate according to power fluctuations would save evaporating duty and ensure a high system electricity efficiency. In the second dynamic period, the *SC* was designed to be fixed at 27.2% (Constant Conversion, CC). The steam flow rate was adapted based on current and *SC*:

$$\dot{n}_{\mathrm{H_2O}} = \frac{\dot{n}_{\mathrm{react}}}{SC} = \frac{I_{\mathrm{stack}}}{2F\cdot SC} \tag{2}$$

The liquid water flow rate ranged between 16 and 85 mL·min^{-1}, and H_2 ranged between 2.4 and 10 L·min^{-1}, while the air was maintained at 66.5 L·min^{-1}. During the CC period, current density also follows wind power fluctuations, as illustrated in Fig. 4. The minimum current density in the CC period is 0.1 A·cm^{-2}, the same as in the CF period. Apart from emphasizing degradation behaviors, such a setting avoids complete feedstock cutoff at OCV during CC operation. Within the CC period, the flow rate and current density were changed every 15 min limited by the steam generator, resulting in 2976 segments. Despite this, an industrial

SOEC system can likely be designed to vary the steam flow rate significantly via pressure control or a steam buffer tank [38,39]. The maximum current decreases or increases between two neighboring segments in the CC period is 0.102 and 0.093 A·cm^{-2}, similar to that in the CF period. The actual *SC* may deviate from 27.2% and the exact value depends on the real-time steam supply and current density.

4. Results

Current, voltage, and temperature are monitored throughout the durability test. This section will first present the electrochemical performance of the SOEC stack before each operation period. Later, the whole voltage and temperature variation processes will be shown. Finally, details that are hard to observe from long-term variations are focused and studied. Data from two short periods is presented to help develop the stack control system in the future.

4.1. Stack performance

The current density-voltage relation (*iV* curve) was used to evaluate SOEC stack electrochemical performance, as its slope represents resistance. Fig. 5 illustrates the *iV* curve before each test period. The solid line presents the average cell voltage, the total stack voltage divided by the number of cells per stack. As previously described, in TSP-1 stacks, several cells form a group, and each group has its average cell voltage. The area around the solid lines illustrates the maximum and minimum group average cell voltages. Voltage difference between groups comes from uneven local heat and mass flow distribution, since two SOEC cells may have different voltages under various gas/current/temperature supplies. The difference between the maximum and minimum group average cell voltage is the stack voltage range. It denotes the performance difference between groups or the inhomogeneity of temperature or gas distribution inside the stack. An equilibrium voltage, or theoretical Open Circuit Voltage (OCV), is marked with a diamond symbol to be compared with the measured OCV at zero current. The theoretical value is estimated based on the experiment temperature and gas flow data

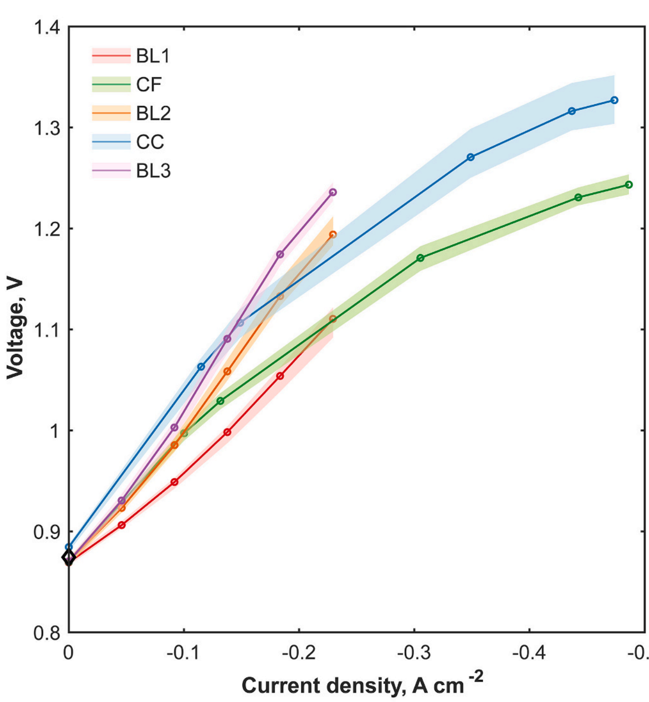

Fig. 5. iV curve of the SOEC stack before each operation period. The solid line represents the average cell voltage, while the area denotes the cell voltage range inside the stack. Diamond at zero current density is the theoretical OCV.

following the Nernst equation:

$$\mathrm{OCV}_{\mathrm{therory}} = \frac{\Delta G}{2F} + \frac{R\overline{T}}{2F} log \frac{p_{H_2}\sqrt{p_{O_2}}}{p_{H_2O}} \quad (3)$$

where G is Gibbs energy, R is gas constant, p is partial pressure, $\overline{T}$ is average temperature of the inlet and outlet stream.

The current density is swept from 0 to 0.24 A·cm^{-2} before each BL period as part of the starting procedure. H_2O, H_2, and air flow continuously and steadily at 40 mL·min^{-1}, 5.67 L·min^{-1}, and 60 L·min^{-1}, respectively. The measured OCV before the three BL test periods is around 870 mV, while the theoretical value is 873 mV. A close match between the measured and theoretical values proves the stack is intact and gas leakage is small throughout the long-term test. The slight OCV deviation could come from uneven temperature distribution inside the stack, contributed by the oven. SOEC testing caused a rise in resistance from BL1 to BL3. More analysis of the degradation process will be discussed in Section 5.

Since the *iV* test procedure was not established at the beginning of the dynamic test, the *iV* curves for the CF and CC tests were extracted from the initial six-hour run, called dynamic *iV* curves. Dynamic and steady *iV* curves should not be compared directly because they follow different operating conditions (temperature, flow rate, etc.). However, experiments with similar test conditions are comparable. The measured OCV for CF and CC is 870 mV and 884 mV, respectively. Both are close to the theoretical values of 873 mV and 871 mV, proving gas tightness before dynamic operation. The CC operation has a larger voltage range than CF and BL, and it increases with the current density. Specifically, there is a voltage range of 19.7 mV and 48.1 mV for CF and CC at the maximum current density, respectively.

4.2. Voltage evolution

The voltage varies with fluctuating current density profiles. Fig. 6 top and bottom depict the average cell voltage and voltage range over the long-term test. The voltage profile was divided into five parts according to the control strategy. BL1, BL2, and BL3 encounter steady voltage rises, while CF and CC encounter fluctuations.

In BL1, the average cell voltage starts at 1.12 V and increases to 1.14 V. The voltage range drops from 29.3 mV to 24.7 mV. The voltage in BL2 rises from 1.19 V to 1.20 V, and the voltage range drops from 28.5 mV to 27.2 mV. In BL3, the voltage climbed from 1.22 V to 1.23 V, and the voltage range was maintained at around 19 mV. BL2 had similar voltage ranges to BL1 but different voltage ranges from BL3. Since BL2 and BL3 operate after CF and CC, the temperature or mass flow distribution inside the stack is assumed to remain constant after CF.

During CF operation, the voltage rises with fluctuation. Because of degradation, the voltage for the same current density increases. For example, the SOEC voltage of 0.10 A·cm^{-2} is 0.99 V at the beginning of CF operation but 1.03 V at the end. There is no significant difference in degradation rate regardless of current density. The voltage range under CF operation is lower than BL, with an average value of 16.8 mV and a standard deviation of 4.8 mV. Full-load operation expands the voltage range. 0.5 A·cm^{-2} operation yields a 25 mV voltage range, while 0.1 A·cm^{-2} gives 11 mV. Voltage fluctuations are more pronounced in the high-voltage section. It could be attributed to concentration resistance variations, uneven temperature distribution, short term uneven local contact, etc.

A degradation trend also appeared during the CC operation period. The voltage of 0.1 A·cm^{-2} was 1.04 V initially and 1.06 V at the end of the CC test. The full-load voltage even becomes higher than the thermoneutral voltage V_{tn}, turning SOEC from endothermic into exothermic operation. CC has a broad and oscillating voltage range. The maximum voltage range is 80.3 mV for CC but 32.5 mV for CF. There is an average voltage range of 26.8 mV for CC, which is 1.6 times above CF and 1.06 times above BL1. Notably, the voltage range in the subsequent BL3 test

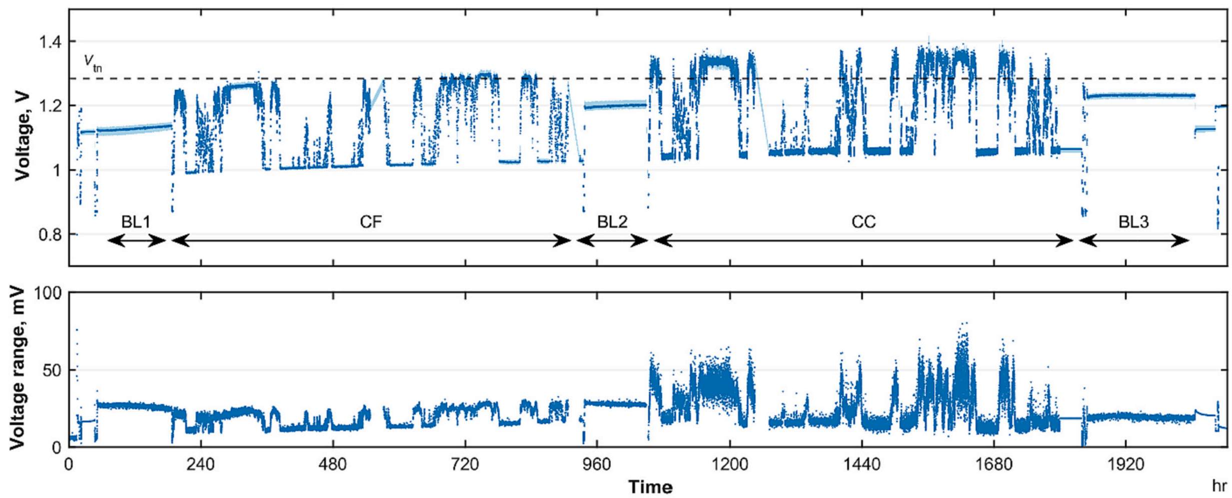

Fig. 6. Voltage evolution during the 2104 h test. The scatter and dash lines in the top figure denote the average cell voltage and the thermoneutral voltage V_{tn}, respectively. The voltage range is shown as an area in the top figure and a scatter in the bottom figure.

was reduced by 20.6% compared to BL2, which implies that CC operation might minimize group differences. Meanwhile, the stable and successful BL3 operation proved the stack worked without losing performance, even after an offensive CC operation.

Overall, the voltage test results reveal the stack is degrading in both steady and dynamic operation. Within the CF and CC period, the stack delivers 618 and 612 Nm^3 H_2, with an average power consumption of 2.25 and 2.72 $kWh{\cdot}Nm^{-3}$ H_2. The initial degradation of the fresh stack accounts for most of the degradation, and more relative discussions will be presented in Section 5. Inhomogeneity in multi-physics fields is not crucial in CF, but critical in CC. No sudden voltage drop was observed, which means the SOEC stack can withstand large fluctuations in power input from e.g. wind energy in both CF and CC operations.

4.3. Temperature evolution

Similar to voltage, temperature exhibits a clear boundary when switching operating strategies. The average temperature and the temperature difference ΔT between the inlet and outlet are shown in Fig. 7. A negative temperature difference means the SOEC is endothermic.

$$\Delta T = T_{out} - T_{in} \tag{4}$$

The average temperature remains stable during a steady period but fluctuates during a dynamic period. It started at 715.3 °C and kept increasing throughout the test. At the end of BL1, BL2, and BL3, the temperatures reached 716.0 °C, 716.5 °C, and 716.7 °C, respectively. Temperature development in BL periods is minimal. In the meantime, the stack is endothermic, and its temperature difference varies from −2.55 °C to −2.35 °C (BL1), −1.65 °C (BL2), and − 1.45 °C (BL3). More ohmic heat was generated by degradation, which reduced the temperature drop between the stack inlet and outlet.

The temperature was positively correlated to the current density during the CF period, but negatively correlated to the current density during the CC period. When the current density increased from 0.1 $A{\cdot}cm^{-2}$ to 0.5 $A{\cdot}cm^{-2}$, the average temperature under CF operation increased by ~2 °C while that under CC operation decreased by ~17 °C. Substantial temperature variation during the CC period could be attributed to the pre-heater, which has a constant duty.

Besides, the temperature of the CC period is more volatile than of the CF period. The maximum temperature variation amplitude is 6.0 °C and 18.1 °C for the CF and CC periods, respectively. A flexible steam generator and preheater that adjust steam inlet temperature could reduce temperature fluctuation under the CC operation strategy. In fact, because of the time lag of the steam generator used in the experiment,

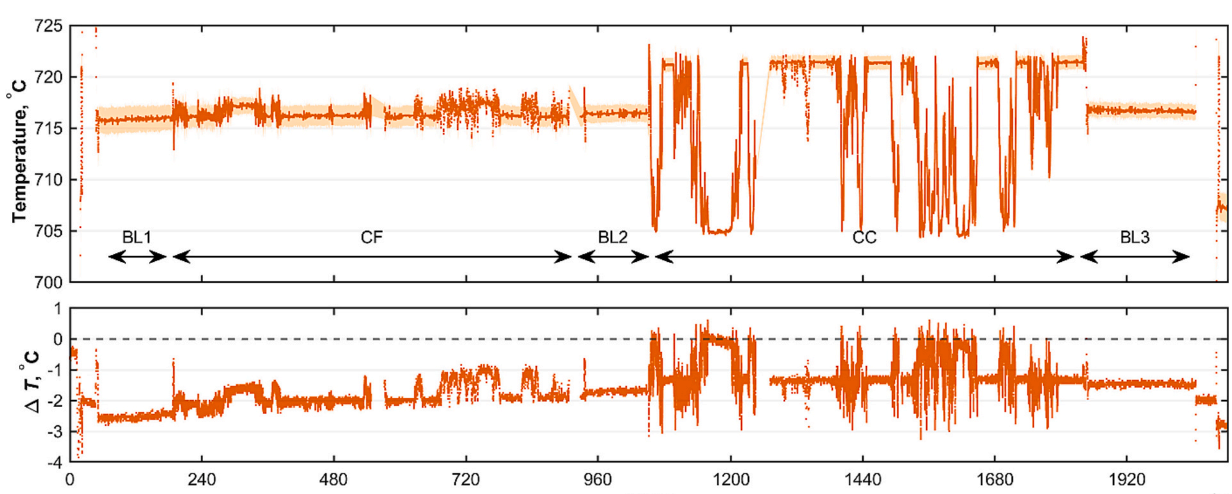

Fig. 7. Temperature evolution during the 2104 h test. The scatter surrounded by an area in the top figure denotes the average temperature $\overline{T}$ and the inlet/outlet temperature. The temperature difference ΔT is shown as a scatter in the bottom figure. Dash line at zero ΔT is marked as reference.

the CC operation was relaxed to 15 min per segment instead of 5 min per segment. The unstable vapor temperature challenges the stack's robustness without proper temperature control. Despite this, the stack is strong and has withstood challenging circumstances with outstanding robustness.

4.4. Dynamic response

A closer look at the dynamic evolution details helps to understand the SOEC pattern under wind power fluctuation. SOEC experimental results are explored hourly to reveal the coupling between multiple physical fields, including flow rate, resistance, voltage, and temperature. This paper presents two short periods for further analysis: the stepwise variation and the dynamic variation. The test data for the two periods are shown in Fig. 8 and Fig. 9, respectively.

In the first short period, the current density is increased and held every 5 min, while data is recorded every minute. The procedure was tested three times before every BL period to extract *iV* curves (Fig. 5). Fig. 8 compares the current densities, voltages, and temperatures of the three tests. Since the current density setup for all tests is the same, only one is illustrated.

Each time the current density steps up, the voltage jumps to another value immediately, followed by a slow variation. The magnitude of the voltage jump is related to the present resistance and degradation progress. After the step change, voltage variation is controlled by temperature. For example, during five minutes where the current density is kept at 91.7 mA·cm^{-2}, the average stack temperature decreases by 0.85 °C, and the voltage increases by 12.5 mV (BL1), 11.7 mV (BL2), and 15.4 mV (BL3). Proper temperature control that minimizes temperature drop could reduce electrolysis power consumption by costing additional external electric heat. The trade-off needs further investigation at the system level.

As the current density and voltage increase, the temperature decreases first and recovers toward the initial 717 °C. However, BL3 has the highest final temperature in these periods because of additional joule heat introduced by degradation. Besides, the stack temperature recovered to its initial value when the voltage reached these corresponding voltages. Theoretically, the stack becomes heat-balanced at thermoneutral voltage. Here, the oven supplies additional heat to the stack, balancing heat at a lower voltage. Further, no sudden temperature change was recorded since the thermal inertia smooths the temperature variation. The system component is easier to control with a stable outlet temperature. Integrating SOEC with downstream hydrogen storage or chemical production systems could become seamless.

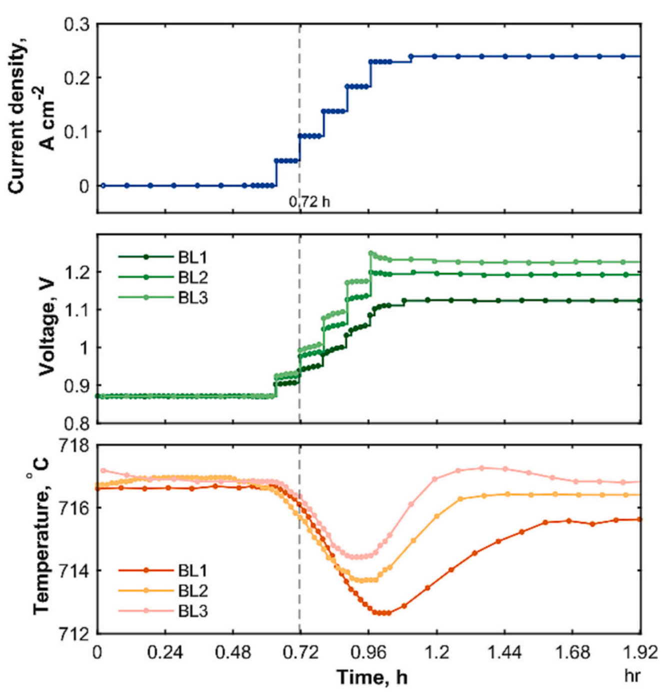

Fig. 8. Dynamic response of the average cell voltage (middle) and stack average temperature (bottom) under stepwise current density variation (top). Dash line at 0.72 h is marked as reference.

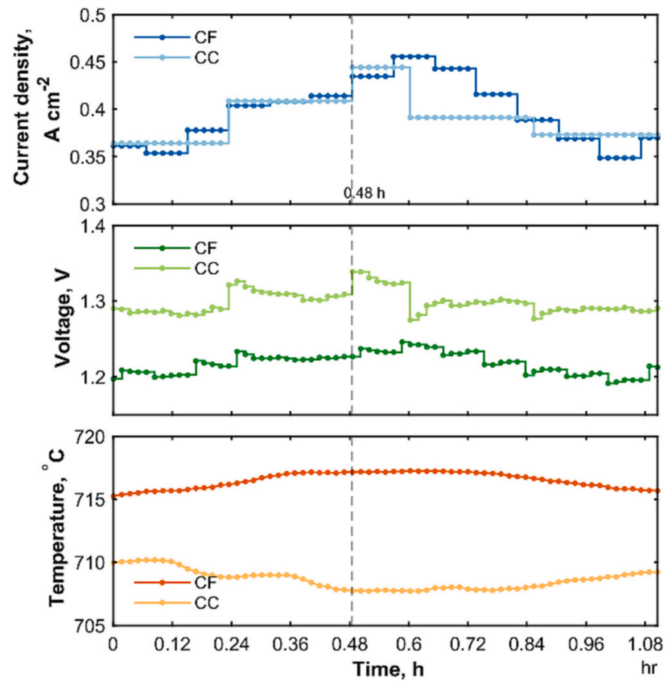

Fig. 9. Dynamic response of the average cell voltage (middle) and stack average temperature (bottom) under stepwise current density variation (top). The dash line at 0.48 h is marked as reference.

The second period selected time with CF and CC operations corresponding to the same part of the wind power fluctuations profile. Fig. 9 illustrates voltage and temperature response under current density and gas flow variation. Following an increase from 0.35 A·cm^{-2} to 0.45 A·cm^{-2}, the current density returned to 0.35 A·cm^{-2} at the end of this short period. The current density changed every five minutes in the CF period and every fifteen minutes in the CC period. The two current density curves do not overlap due to control frequency differences. Another consequence is that CF usually has a higher current density in the selected period.

CF and CC have similar voltage responses patterns. Even though the CF and CC voltages develop in similar trends, their amplitudes are different. CF moves from 1.20 V to 1.24 V and back to 1.21 V. In CC, the voltage increases from 1.29 V to 1.34 V and then returns to 1.29 V. If the current density rises and stays constant, the voltage changes abruptly to a high level and then drops slowly. Conversely, the voltage drops to a low point and increases gradually. For instance, the current density increased at 0.48 h by 30 and 26 mA·cm^{-2} for CF and CC strategies, respectively. After that, the current density was maintained at 444 and 435 mA·cm^{-2}, respectively. In response, the voltage increases by 10 mV before slipping by 5 mV in the CF period. Instead, the CC strategy raises the voltage by 30 mV and drops it by 15 mV. Temperature variation is negligible at around 0.48 h for both operation strategies. Overall, stack temperature variation is milder in CF operations than in CC operations. Specifically, the temperature variation amplitude in the dynamic short period is 1.4 °C and 1.5 °C for CF and CC operations, respectively.

5. Discussion

SOEC stack performances, including degradation, electric efficiency, and heat balance, are derived from experimental data and analyzed sequentially. Degradation analysis results illustrate the group degradation rate during each operation period. Electric efficiency analysis compares the operation strategies without degradation effects. Heat balance analysis reveals the external heat supply and will inspire the development of heat management procedures at the system level.

5.1. Degradation

It is essential to emphasize degradation since it increases resistance and decreases efficiency. Fig. 10 illustrates the average cell voltage and area-specific resistance (ASR) when SOEC operated at 0.24 A·cm^{-2}. The groups' degradation rate (DR) during BL1, BL2, and BL3 periods is shown at the bottom. ASR and DR are calculated by:

$$ASR = \frac{V - OCV_{theory}}{i} \quad (5)$$

$$DR_V = \frac{V_{end} - V_{start}}{t_{end} - t_{start}}, DR_{ASR} = \frac{ASR_{end} - ASR_{start}}{t_{end} - t_{start}} \quad (6)$$

Initially, the voltage at 0.24 A·cm^{-2} is 1.12 V, and the ASR is 1.04 Ω·cm^2. Since the traditional piecewise linear function is not accurate, the voltage degradation at 0.24 A·cm^{-2} is fitted with a logarithmic function:

$$V_{deg} = 0.05885 ln(t + 287.3) - 0.3401 \quad (7)$$

where t is time in hour. The stack degraded rapidly at the beginning and leveled off at the end. The stack average DR of BL1, BL2, and BL3 is 107.7, 81.0, and 40.4 mV·kh^{-1}, respectively. This is expected since similar trends and development have been observed in many durability tests [40,41]. Rapid degradation in the first 500–1000 h is often seen in SOEC cells or stacks. Such phenomena have been proposed to be related to the initial Ni/YSZ electrode microstructure re-organization, though the exact mechanism behind it is still under discussion [40,42]. The evolution of the average cell voltage during the two dynamic operation periods follows the trend defined by the three steady operation periods. This indicates that the dynamic operation conducted in this test did not introduce additional degradation.

There is a difference in DR between the groups. Degradation in the top group was 58% faster than in the middle group during the BL1 period. The other groups have similar degradation rates. Ideally all cells in the stack should have similar initial performance since they are produced in the same batch. The difference in degradation rate could be attributed to the imbalance in local current, gas, or temperature distribution. During the BL2 period, degradation became inhomogeneous within the stack. The middle group G07 degraded at 31.8 mV·kh^{-1} (0.13 Ω·cm^2·kh^{-1}, 2.8%·kh^{-1}). Group G08 was next to G07 but degraded faster by 118 mV·kh^{-1} (0.49 Ω·cm^2·kh^{-1}, 10.5%·kh^{-1}). Degradation during the BL3 period is minimal. G13 at the top degrades fastest with a DR of 58.7 mV·kh^{-1} (0.24 Ω·cm^2·kh^{-1}, 5.2%·kh^{-1}). Groups have a similar degradation rate in BL3. It could be inferred that all cells have reached stable degradation. Top group G13 has the fastest degradation rate in BL3, while bottom group G01 has the slowest. Optimizing gas flow channels, concentration/temperature distribution, and contact resistance might reduce degradation.

5.2. Power regulation and efficiency

Voltage variation in dynamic operation periods involves fluctuation and degradation. However, degradation causes the voltage to non-linear increase and blurs the voltage fluctuation. To compare the direct effect of CF and CC operation under power fluctuation, their voltage is calibrated by removing degradation:

$$V_{calibrated} = V - V_{deg} \quad (8)$$

Calibrated voltage, electric efficiency, and corresponding histogram are shown in Fig. 11 top. Without degradation, the fundamental differences between CF and CC control strategies originate from flow rate, sensible heat supply, resistance, and dynamic behavior. If the dynamic control strategies are conducted at another degradation stage, they should have a similar calibrated voltage to this work since the fundamental difference still exists. SOEC electrical efficiency is directly related to voltage:

$$\eta_{stack,LHV} = \frac{LHV \cdot \dot{n}_{react}}{W_{el}} = \frac{LHV \cdot I/2F \cdot \eta_{Faraday}}{IV} = \frac{LHV \cdot \eta_{Faraday}}{2FV} \quad (9)$$

where W_{el} is electric work, and LHV is hydrogen low heating value. $\eta_{Faraday}$ is Faraday efficiency, which is 100% for SOEC [43].

The voltage variation amplitude in the CC period is more significant than in the CF period, regardless of calibration. After calibration, the voltage in CC operation is 2% higher than CF at full load power supply.

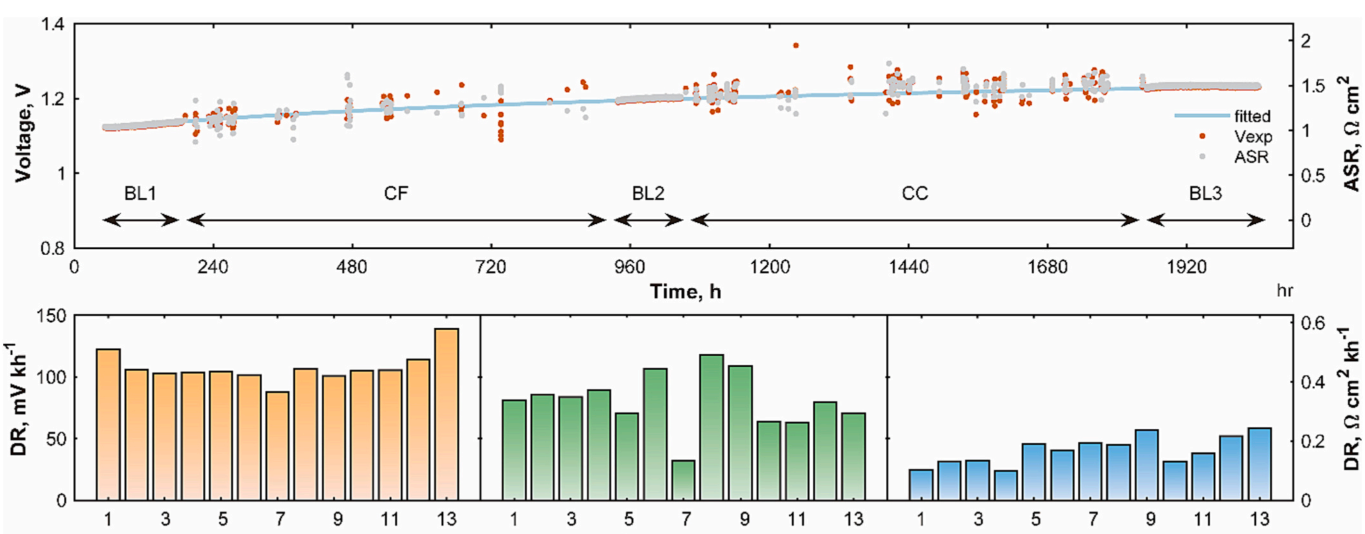

Fig. 10. Evolution of the average cell voltage when the stack was operated at 0.24 A·cm^{-2} during the 2104 h test (top). The bottom figure is the DR in BL1 (left), BL2 (center), and BL3 (right) periods.

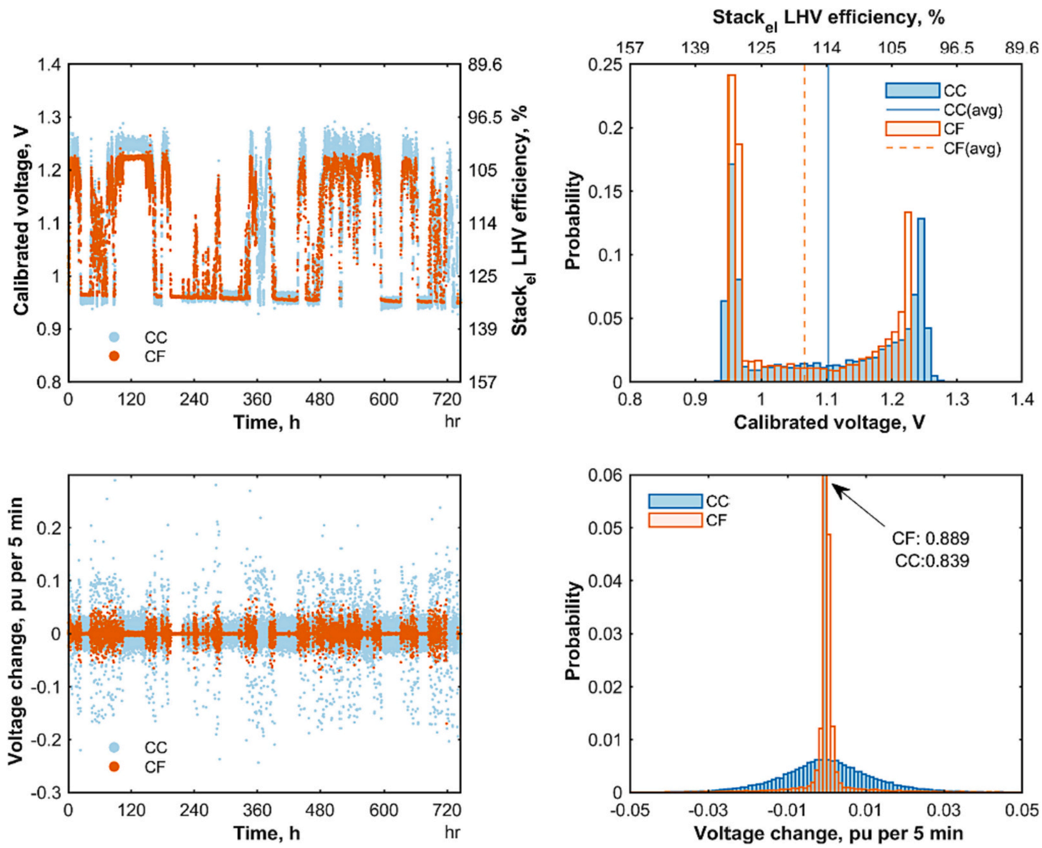

Fig. 11. Calibrated voltage in CC and CF operation (top left) and their histogram (top right). Voltage changes in CC and CF operation (bottom left) and their histogram (bottom right).

CF and CC operations have similar voltage responses when power is insufficient. The calibrated voltage for the minimum current density of 0.1 A·cm^{-2} is close, with values of 0.95 V for CC and 0.96 V for CF. Like the current density, the voltage in both CF and CC periods has two peaks at both ends of their histogram. CF peaks at 0.95 and 1.22 V, while CC peaks at 0.95 and 1.24 V. Hence, the average voltage for CF and CC periods is 1.07 and 1.10 V, respectively. Stack electric efficiency is inversely proportional to voltage. CF and CC operations have an average electric efficiency of 120.5% and 116.5%, respectively. Despite this, electricity for steam generation could be saved under CC operation. Further investigation into steam generators and SOEC energy consumption is needed for both operation strategies at the system level.

Corresponding to wind speed fluctuations, the voltage change at two adjacent time segments is analyzed here. The value and histogram for voltage changes are shown in Fig. 11 bottom. Their unit is pu per·5 min with thermoneutral voltage as a nominal value. The voltage varies more with the CC strategy. The maximum voltage change for CC operation is 0.68 pu per·5 min, and for CF, it is 0.17 pu per·5 min. There is a slight possibility of rapid voltage changes, but it cannot be ignored. The probability of a voltage changing more significant than 0.01 pu per·5 min is 6.5% for CC operation and 1.6% for CF operation. Such a probability corresponds to 23.8 days and 5.7 days in one year. Despite the substantial deviation, the stack operated normally, proving its robustness.

Insufficient external heat supply reduces the stack temperature, especially during the CC period, as shown in Section 4. Thus, the external heat shortage raises resistance, increases voltage, and decreases electric efficiency. If a more flexible thermal management system was deployed instead of the constant duty pre-heater, a stable temperature, a lower voltage, and a higher electric efficiency could be achieved. The detailed heat balance analysis is presented next to inspire the flexible thermal management system design.

5.3. Heat balance

Water/steam splitting is an endothermic reaction below the thermoneutral voltage. External heat is needed to keep the stack warm, minimize the resistance, and reduce the temperature gradient. During the test, the steam was pre-heated, and the stack was placed in an electric oven. The pre-heater and oven are external heat sources. However, many stacks are installed in an industrial SOEC hot box, and the oven design would be space-consuming and less efficient. Instead, the stack could be placed on a hot plate for direct electric heat transfer. Hot plate and pre-heater duty can be controlled, but the amount must be quantified beforehand.

The heat balance estimates external heat Q_{ext} contributed by oven:

$$Q_{\text{react}} + W_{\text{el}} + Q_{\text{in}} + Q_{\text{out}} + Q_{\text{ext}} = 0 \tag{10}$$

$$Q_{\text{react}} = \dot{n}_{\text{react}} \Delta_r H = \frac{I_{\text{stack}} \Delta_r H}{2F} \tag{11}$$

$$W_{\text{ele}} = I_{\text{stack}} V_{\text{stack}} \tag{12}$$

$$Q_j = \left(T_j - \overline{T}\right) \sum_i \dot{n}_i C p_{i,j}, \quad i \in \{H_2, O_2, H_2O, N_2\}, j \in \{\text{inout}\} \tag{13}$$

where Q_{react} is reaction heat, Q_{in} and Q_{out} are heat flow input and output, N_{cps} is the number of cells in stack, $\dot{n}_i$is the mole flow rate for component i, and Cp is the heat capacity. Using experiment data, including temperature, current density, voltage, and flow rate, to solve the heat balance equation will get the external heat duty provided by the oven. Joule heat caused by degradation could obscure the thermal variation caused by the operation. Thus, the calibrated external heat removed the additional joule heat by substituting $V_{calibrated}$ for experiment data V_{exp} in the heat balance equation. The evolution of external heat over time before and after calibration is shown in Fig. 12 top. The histogram of external heat during the CF and CC periods is presented in the middle, and the calibrated external heat versus current density is shown at the bottom.

The stack degradation increases resistance and releases more ohmic heat. Because of it, the external heat supply gradually decreases from 339 W to 311 W (BL1), 178 W (BL2), and 125 W (BL3). Degradation is a major contributor to the internal heat balance development. Without degardation, the calibrated external heat during the steady period (BL1, BL2, and BL3) is almost stable between 338 and 350 W.

External thermal energy consumption differs significantly between CF and CC operation strategies. More external heat is consumed by the CF strategy than by the CC strategy. The calibrated external heat requirement is 250–380 W for CF operation and 100–400 W for CC operation. The average calibrated external heat is 299 and 254 W for CF and CC strategies, respectively. CC strategy saved 15% external heat but consumed more electricity for steam splitting. CF operation has stable temperature distribution and higher electric efficiency but requires more external heat.

The histogram of the calibrated external heat during the CF period has two peaks, one at 275 W (45%) and the other at 345 W (6%). Three peaks were found on the histogram of the CC period: 165 W (4%), 275 W (22%), and 325 W (5%). This comes from the non-linear relationship between calibrated external heat and current density. The calibrated external heat and current density exhibit an upward convexity relationship in CF operation. Meanwhile, the calibrated external heat under CC operation shows a wave relationship with the current density. Further, the thermal inertia of the stack expands the duty distribution.

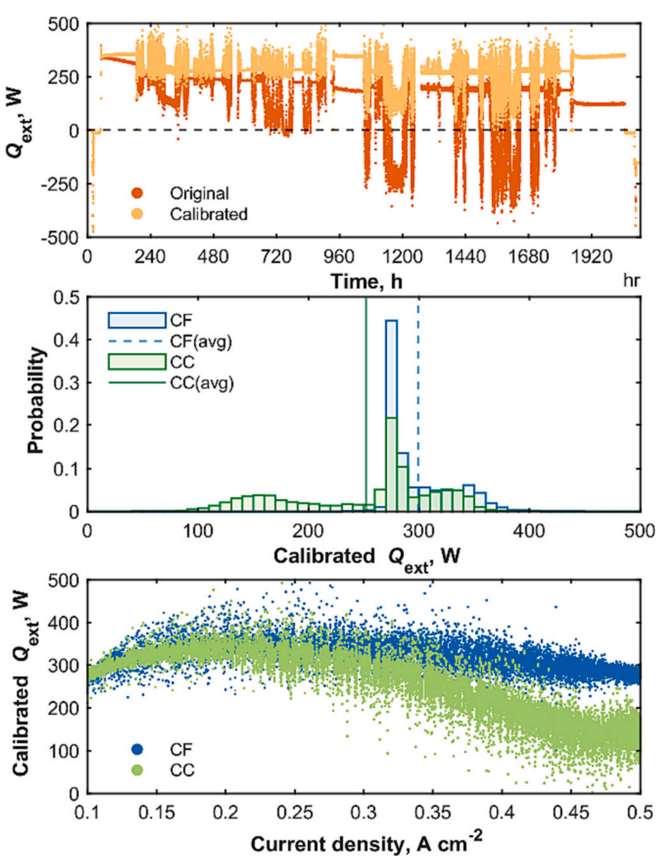

Fig. 12. Evolution and probability of the Q_{ext} during the 2104 h test. The top one plots the development of Q_{ext} w/wo calibration. The middle one is the histogram of calibrated Q_{ext}. The bottom one shows the Q_{ext} verse current density.

For example, the standard deviation for calibrated external heat at 0.45 A·cm^{-2} is 31.4 and 67.7 W for CF and CC periods, respectively. CC operation has a broader distribution because it has less steam and lower thermal inertia.

The non-linear relationship and thermal inertia make it challenging to conduct SOEC control strategies at the system level. System development is intended to minimize energy consumption and improve economic performance. SOEC systems rely on internal hot plates, preheaters, steam generators, and heat exchanger networks to supply and recover thermal energy. Non-linear external heat demand will complicate system control, heat management, and optimization. Besides, widespread Q_{ext} indicates that dynamic operation differs from stable operation. System optimization should be conducted based on dynamic simulation to reveal optimal energy and economic performance, even though technical obstacles will exist.

6. Conclusion and Outlook

This work conducted a 2104 h stack test to verify a Wind-SOEC coupled system and clarify the impact of fluctuating wind power on the SOEC stack. A 75-cell state-of-the-art TSP-1 stack from Topsoe was employed. A real-life wind profile from a wind farm on the Danish Island of Bornholm was down-scaled to ~7 kW for the TSP-1 stack. The test comprised three short-term steady operation periods (BL1, BL2, and BL3) plus two 744-h dynamic operation periods (CF and CC) in the order of BL1-CF-BL2-CC-BL3. A constant current density of 0.24 A·cm^{-2} was set for the steady operation period. In both dynamic periods, the stack followed the December wind profile with a fluctuating current density between 0.1 and 0.5 A·cm^{-2}. Constant flow and constant conversion flow rate control strategies were deployed in CF and CF periods, respectively. The CF strategy maintained the inlet flow rate, while the CC strategy maintained the conversion ratio and updated the steam flow rate according to the current density.

The SOEC stack delivered 618 and 612 Nm^3 H_2 during the CF and CC periods, respectively. 2.25 kWh·Nm^{-3} H_2 (CF) and 2.72 kWh·Nm^{-3} H_2 (CC) of electricity were consumed by the stack. Stack voltage increased from 1.12 to 1.23 V for the entire process. The degradation rate decreased from 107.7 mV·kh^{-1} (BL1) to 40.4 mV·kh^{-1} (BL3). Meanwhile, power, temperature, and stream composition fluctuations didn't introduce additional degradation. Thermal energy management is essential for SOEC stability and system efficiency. Energy analysis reveals that transient heat-duty variation didn't affect stack strength. Stack performance under CF and CC control strategies was compared and analyzed by removing degradation effects. Voltage is more sensitive to wind power variation under the CC control strategy. Meanwhile, CC periods require less external heat to keep heat balance. More system simulations, analyses, or experiments should be conducted to compare and evaluate CF and CC in practice concerns. In conclusion, TSP-1 is robust and flexible enough to produce hydrogen using fluctuating wind power.

SOEC commercialization requires profound economic performance. All potential methods and scenarios should be evaluated from economic perspectives. Grid connection, external heat supply, SOEC development, and other technologies could be integrated into SOEC systems and reduce hydrogen production costs. Dynamic or pseudo-transient models are needed to simulate system response to fluctuating wind power. Tech-economic analyses and optimization will be conducted to compare CF and CC operation strategies at the system level. In-depth research on SOEC degradation under dynamic conditions is worthwhile for (1) durability tests at different SOEC operating conditions (temperature, current density, conversion ratio), (2) electrochemical numerical model development based on degradation mechanisms, (3) system development to enhance flexibility and resiliency, and (4) joint optimization of control strategies, system design, SOEC operating conditions, etc. In the future, SOEC will become one of the fundamental utilities for green hydrogen production and global environmental sustainability.

CRediT authorship contribution statement

Hua Liu: Writing – review & editing, Writing – original draft, Visualization, Software, Methodology, Data curation. **Jens Høgh:** Writing – review & editing, Validation, Software, Methodology, Investigation, Data curation. **Peter Blennow:** Writing – review & editing, Validation, Methodology, Investigation. **Xiufu Sun:** Writing – review & editing, Software, Methodology, Investigation. **Yi Zong:** Writing – review & editing, Data curation. **Ming Chen:** Writing – review & editing, Validation, Resources, Project administration, Methodology, Investigation, Funding acquisition.

Declaration of competing interest

The authors declare that they have no known competing financial interests or personal relationships that could have appeared to influence the work reported in this paper.

Data availability

The data that has been used is confidential.

Acknowledgement

This work was supported by the projects “Towards Solid Oxide Electrolysis Plants in 2020” (ForskEL no. 2015-1-12276) and “Efficient Power2Gas Combining SOEC and Biomass Gasification” (EUDP no. 64017-0011). Ming Chen further acknowledges the project “Integrated Energy Conversion and Control for Smart and Efficient Electrolysis Systems (IECC)” (IFD project no. 8087-00019B) for support in finalizing the manuscript.

References

[1] N. Batini, I.W.H. Parry, P. Wingender, Climate mitigation policy in Denmark: A prototype for other countries, n.d. https://www.imf.org/en/Publications/WP/Issues/2020/11/12/Climate-Mitigation-Policy-in-Denmark-A-Prototype-for-Other-Countries-49882 (accessed April 23, 2023).

[2] Frederiksen M, Ellemann-Jensen J, Rasmussen LL. Ansvar for Danmark - Det politiske grundlag for Danmarks regering. 2022.

[3] Yaramasu V, Wu B, Sen PC, Kouro S, Narimani M. High-power wind energy conversion systems: state-of-the-art and emerging technologies. P IEEE 2015;103:740–88. https://doi.org/10.1109/jproc.2014.2378692.

[4] Hevia-Koch P, Jacobsen HK. Comparing offshore and onshore wind development considering acceptance costs, Energ. Policy 2019;125:9–19. https://doi.org/10.1016/j.enpol.2018.10.019.

[5] D.E. Agency. Denmark’s Energy Islands | Energistyrelsen. 2023. https://ens.dk/en/our-responsibilities/energy-islands/denmarks-energy-islands (accessed April 23, 2023).

[6] Dicorato M, Forte G, Pisani M, Trovato M. Guidelines for assessment of investment cost for offshore wind generation. Renew Energy 2011;36:2043–51. https://doi.org/10.1016/j.renene.2011.01.003.

[7] Weimann L, Gabrielli P, Boldrini A, Kramer GJ, Gazzani M. Optimal hydrogen production in a wind-dominated zero-emission energy system. Adv Appl Energy 2021;3:100032. https://doi.org/10.1016/j.adapen.2021.100032.

[8] Joung T-H, Kang S-G, Lee J-K, Ahn J. The IMO initial strategy for reducing Greenhouse Gas(GHG) emissions, and its follow-up actions towards 2050. J Int Marit Saf, Environ Aff, Shipp 2020;4:1–7. https://doi.org/10.1080/25725084.2019.1707938.

[9] Park SI, Kim JH, Le TD, Lee DH, Kim DJ, Yoon YS, et al. Analysis of losses within SMES system for compensating output fluctuation of wind power farm. Prog Supercond Cryog 2014;16:57–61. https://doi.org/10.9714/psac.2014.16.4.057.

[10] You S, Reissner R, Imboden C, Bourasseau C, Marcuello P, Greenhalgh D, et al. Facilitating water electrolysers for electricity-grid services in Europe through establishing standardized testing protocols. Clean Energy 2020;4:zkaa015. https://doi.org/10.1093/ce/zkaa015.

[11] Hauch A, Küngas R, Blennow P, Hansen AB, Hansen JB, Mathiesen BV, et al. Recent advances in solid oxide cell technology for electrolysis. Science 2020;370. https://doi.org/10.1126/science.aba6118.

[12] Salehmin MNI, Husaini T, Goh J, Sulong AB. High-pressure PEM water electrolyser: a review on challenges and mitigation strategies towards green and low-cost hydrogen production. Energ Conver Manage 2022;268:115985. https://doi.org/10.1016/j.enconman.2022.115985.

[13] Mogensen MB, Chen M, Frandsen HL, Graves C, Hansen JB, Hansen KV, et al. Reversible solid-oxide cells for clean and sustainable energy. Clean Energy 2019;3:175–201. https://doi.org/10.1093/ce/zkz023.

[14] Sun X, Bonaccorso AD, Graves C, Ebbesen SD, Jensen SH, Hagen A, et al. Performance characterization of solid oxide cells under high pressure. Fuel Cells 2015;15:697–702. https://doi.org/10.1002/fuce.201500020.

[15] Sun Y, Zheng W, Ji S, Sun A, Shuai W, Zheng N, et al. Dynamic behavior of high-temperature CO2/H2O CO-electrolysis coupled with real fluctuating renewable power. Sustain Energy Technol Assess 2022;52:102344. https://doi.org/10.1016/j.seta.2022.102344.

[16] Lebbal ME, Lecœuche S. Identification and monitoring of a PEM electrolyser based on dynamical modelling. Int J Hydrogen Energy 2009;34:5992–9. https://doi.org/10.1016/j.ijhydene.2009.02.003.

[17] Brauns J, Turek T. Alkaline water electrolysis powered by renewable energy: a review. Process 2020;8:248. https://doi.org/10.3390/pr8020248.

[18] Rakousky C, Reimer U, Wippermann K, Kuhri S, Carmo M, Lueke W, et al. Polymer electrolyte membrane water electrolysis: restraining degradation in the presence of fluctuating power. J Power Sources 2017;342:38–47. https://doi.org/10.1016/j.jpowsour.2016.11.118.

[19] Zhang C, Wang J, Ren Z, Yu Z, Wang P. Wind-powered 250 kW electrolyzer for dynamic hydrogen production: a pilot study. Int J Hydrogen Energy 2021;46:34550–64. https://doi.org/10.1016/j.ijhydene.2021.08.029.

[20] Fu Q, Schefold J, Brisse A, Nielsen JU. Durability testing of a high-temperature steam Electrolyzer stack at 700°C. Fuel Cells 2014;14:395–402. https://doi.org/10.1002/fuce.201300150.

[21] Sun Y, Hu X, Gao J, Han Y, Sun A, Zheng N, et al. Solid oxide electrolysis cell under real fluctuating power supply with a focus on thermal stress analysis. Energy 2022;261:125096. https://doi.org/10.1016/j.energy.2022.125096.

[22] Liu H, Clausen LR, Wang Ligang, Chen M. Pathway toward cost-effective green hydrogen production by solid oxide electrolyzer. Energ Environ Sci 2023. https://doi.org/10.1039/d3ee00232b.

[23] Hauch A, Blennow P. Solid oxide electrolysis cells – interplay between operating conditions, fuel electrode overpotential and degradation. Solid State Ion 2023;391:116127. https://doi.org/10.1016/j.ssi.2022.116127.

[24] Subotić V, Hochenauer C. Analysis of solid oxide fuel and electrolysis cells operated in a real-system environment: state-of-the-health diagnostic, failure modes, degradation mitigation and performance regeneration. Prog Energ Combust 2022;93:101011. https://doi.org/10.1016/j.pecs.2022.101011.

[25] Petipas F, Fu Q, Brisse A, Bouallou C. Transient operation of a solid oxide electrolysis cell. Int J Hydrogen Energy 2013;38:2957–64. https://doi.org/10.1016/j.ijhydene.2012.12.086.

[26] Sanz-Bermejo J, Muñoz-Antón J, Gonzalez-Aguilar J, Romero M. Part load operation of a solid oxide electrolysis system for integration with renewable energy sources. Int J Hydrogen Energy 2015;40:8291–303. https://doi.org/10.1016/j.ijhydene.2015.04.059.

[27] N.P. AS, Nord Pool, (n.d.). https://www.nordpoolgroup.com/en/ (accessed June 1, 2023).

[28] D.E. Agency. Denmark is establishing a new bidding zone at the Bornholm Energy Island | Danish energy agency. 2024. https://via.ritzau.dk/pressemeddelelse/13764177/denmark-is-establishing-a-new-bidding-zone-at-the-bornholm-energy-island?publisherId=13560521&lang=da (accessed January 29, 2024).

[29] Zecchino A, Prostejovsky AM, Ziras C, Marinelli M. Large-scale provision of frequency control via V2G: the Bornholm power system case. Electr Pow Syst Res 2019;170:25–34. https://doi.org/10.1016/j.epsr.2018.12.027.

[30] Albadi MH, El-Saadany EF. Wind turbines capacity factor modeling—a novel approach. Ieee T Power Syst 2009;24:1637–8. https://doi.org/10.1109/tpwrs.2009.2023274.

[31] Arrambide I, Zubia I, Madariaga A. Critical review of offshore wind turbine energy production and site potential assessment. Electr Pow Syst Res 2019;167:39–47. https://doi.org/10.1016/j.epsr.2018.10.016.

[32] Küngas R, Blennow P, Heiredal-Clausen T, Nørby TH, Rass-Hansen J, Hansen JB, et al. Progress in SOEC development activities at Haldor Topsøe. Ecs Trans 2019;91:215–23. https://doi.org/10.1149/09101.0215ecst.

[33] Küngas R, Blennow P, Heiredal-Clausen T, Nørby TH, Rass-Hansen J, Moses PG. Lifetime capacity – an important performance metric for SOEC stacks. Ecs Trans 2019;91:2601–11. https://doi.org/10.1149/09101.2601ecst.

[34] Trini M, Hauch A, Angelis SD, Tong X, Hendriksen PV, Chen M. Comparison of microstructural evolution of fuel electrodes in solid oxide fuel cells and electrolysis cells. J Power Sources 2020;450:227599. https://doi.org/10.1016/j.jpowsour.2019.227599.

[35] Drasbæk D, Kungas R, Blennow P, Heiredal-Clausen T, Høgh JVT, Hauch A. A framework for characterizing commercial solid oxide electrolysis stacks using electrochemical impedance spectroscopy and equivalent circuit modeling. Electrochem Soc Trans 2021;103:529–43. https://doi.org/10.1149/10301.0529ecst.

[36] Casteel M, Loughmiller C, Petri R, Westover T, Hartvigsen J, Blennow P, et al. Performance and endurance characterization of a commercial prototypical SOEC stack. In: In: 15th European SOFC & SOE forum, Lucerne Switzerland; 2022.

[37] Hoerlein MP, Riegraf M, Costa R, Schiller G, Friedrich KA. A parameter study of solid oxide electrolysis cell degradation: microstructural changes of the fuel electrode. Electrochim Acta 2018;276:162–75. https://doi.org/10.1016/j.electacta.2018.04.170.

[38] Åström KJ, Bell RD. Drum-boiler dynamics. Automatica 2000;36:363–78. https://doi.org/10.1016/s0005-1098(99)00171-5.

[39] Raphael VSP, Velraj R, Jalihal P. Transient analysis of steam accumulator integrated with solar based MED-TVC system. Desalination 2018;435:3–22. https://doi.org/10.1016/j.desal.2017.12.045.

[40] Sun X, Hendriksen PV, Mogensen MB, Chen M. Degradation in solid oxide electrolysis cells during long term testing. Fuel Cells 2019;19:740–7. https://doi.org/10.1002/fuce.201900081.

[41] Tong X, Hendriksen PV, Hauch A, Sun X, Chen M. An up-scalable, infiltration-based approach for improving the durability of Ni/YSZ electrodes for solid oxide cells. J Electrochem Soc 2020;167:024519. https://doi.org/10.1149/1945-7111/ab6f5c.

[42] Yang Y, Tong X, Hauch A, Sun X, Yang Z, Peng S, et al. Study of solid oxide electrolysis cells operated in potentiostatic mode: effect of operating temperature on durability. Chem Eng J 2021;417:129260. https://doi.org/10.1016/j.cej.2021.129260.

[43] Schefold J, Brisse A, Zahid M. Electronic conduction of Yttria-stabilized zirconia electrolyte in solid oxide cells operated in high temperature water electrolysis. J Electrochem Soc 2009;156:B897. https://doi.org/10.1149/1.3138701.